

Structural phase transition at high temperatures in solid molecular hydrogen and deuterium

T. Cui^{1,2}, Y. Takada², Q. Cui¹, Y. Ma¹, G. Zou¹

¹National Lab for Superhard Materials, Jilin University, Changchun 130023, P. R. China

²Institute for Solid State Physics, University of Tokyo, Kashiwa, Chiba 277-8581, Japan
(28 Dec 2000)

We study the effect of temperature up to 1000K on the structure of dense molecular *para*-hydrogen (*p*-H₂) and *ortho*-deuterium (*o*-D₂), using the path-integral Monte Carlo method. We find a structural phase transition from orientationally disordered hexagonal close packed (hcp) to an orthorhombic structure of *Cmca* symmetry before melting. The transition is basically induced by thermal fluctuations, but quantum fluctuations of protons (deuterons) are important in determining the transition temperature through effectively hardening the intermolecular interaction. We estimate the phase line between hcp and *Cmca* phases as well as the melting line of the *Cmca* solid. (accepted for publication in Physical Review B)

PACS numbers: 02.70.Ss, 62.50.+p, 64.70.Kb, 64.70.Dv

I. INTRODUCTION

The possibility for hydrogen to undergo a pressure-induced phase transition from a proton-paired insulator to a monatomic metal was first suggested in 1935.¹ Since then a large body of experimental and theoretical works have been done to determine its phase diagram in the pressure (P) and temperature (T) plane. Despite studies at P reported to be as high as 342 GPa,² the tenacious covalent-bond feature of a pair of protons does not allow observation of a monatomic phase so far.

For P up to *ca.* 200GPa, the phase diagram has been investigated by several research groups at the room temperature and below, based on the optical measurement performed in the diamond anvil cell (DAC) devices. By now it is well established that the solid hydrogen exhibits at least three different molecular phases (the phases I–III), although some details are still in dispute.^{3–9} (1) Phase I: At $P < 110$ GPa, each center of the H₂ molecule occupies the lattice site of an hcp structure, but quantum rotational effects overcome librational barriers, leading to an orientationally disordered phase. (2) Phase II or broken-symmetry phase (BSP): At P between 110GPa and 150GPa, anisotropic intermolecular interactions freeze the molecular rotations into an orientationally ordered phase. (3) Phase III or H-A phase: At P above 150 GPa, a third phase is observed, expected to be another kind of orientationally ordered phase.

In 1996, Weir and coworkers gave one of the exciting results. They observed high electrical conductivity in the shock compressed H₂ and D₂ liquids and interpreted it as a transition from a semiconducting to a metallic diatomic fluid at 140 GPa and 3000K.¹⁰ This experiment clearly demonstrates the importance of temperature effects in the search of metallization. For T larger than 5000K, the effects are studied theoretically in the molecular, the dissociated, and the plasma regime of dense H₂.^{11,12} It is, however, still largely unclear how T influences the state

of solid H₂ at T higher than the room temperature. We need to know the phase diagram at this temperature region to connect the liquid state with the low-temperature phases for a comprehensive understanding of dense H₂. Thus we focus our attention on the range of P up to 200GPa and $300\text{K} < T < 1000\text{K}$ in this paper.

In order to study the condensed H₂ phases theoretically, several methods have been adopted at various levels of approximations to the *ab initio* Hamiltonian representing the coupled system of N_a protons and N_a electrons. These include the calculation of electronic energies in the local density approximation (LDA) or its refinements to the density functional theory for a variety of crystal structures with molecular orientations fixed to some particular configuration,^{13–25} and the implementation of *ab initio* molecular dynamics treating protons as classical particles.^{26–28} We should note, however, that the strong quantum nature of light protons requires a more careful quantum-mechanical description of their zero-point motion. In fact, using either the first-principle path-integral molecular dynamics²⁹ or the quantum Monte Carlo (QMC) simulations,^{11,30,31} the calculation treating protons as dynamic quantum particles has already been performed. Although desirable, this approach demands the computer resources very much. Thus, even in a recent paper,²⁹ the calculation is done only with as small as $N_a = 64$. This size of N_a is too small in order to obtain a correct equilibrium structure free from any bias of an initially assumed one through simulations.

A ten times increase in N_a is possible if we approach the problem by adopting the hydrogen molecule as a basic ingredient in simulations rather than the proton-electron mixture. In this approach, the system is reduced to a quantum-mechanical problem of N ($=2N_a$) molecules interacting to each other through an effective intermolecular pair potential V_{pair} . Thus the QMC calculation is implemented only for the nuclear degrees of freedom^{32–37} and the electronic degrees of freedom

are implicitly taken into account in the choice of V_{pair} . In the present paper, we adopt this approach and employ the finite-temperature path-integral Monte Carlo (PIMC) method to investigate both lattice and orientational transitions in the molecular phase with zero-point motions incorporated rigorously. We shall use an empirically determined V_{pair} which is the sum of the Hemley-corrected Silvera-Goldman potential³⁸ and the Runge-scaled Shaefer potential.³³ This choice of V_{pair} is known to give an equation of state in very good agreement with experiment as well as the I/II phase boundaries for both H_2 and D_2 over the whole experimentally investigated range of pressures.³⁷

This paper is organized as follows: We shall explain our theoretical model in more detail in Sec. II, including a review of trials to determine V_{pair} , a description of our choice of V_{pair} , a brief summary of the PIMC method with a constant-pressure ensemble, and some computational details. In Sec. III our results are shown for both solid H_2 and D_2 , indicating a temperature-induced solid-solid structural phase transition. The structure of the new high-temperature phase, the solid-liquid phase transition, and the phase diagram are also given here. Section IV contains a discussion on the role of zero-point motion of protons in the solid-solid structural phase transition and finally in Sec. V we summarize our results.

II. THEORETICAL MODEL

A. Molecule base

Within the temperature and pressure range that a molecule can be regarded as a basic ingredient, a quantum molecular solid can be described by the Hamiltonian H_{nuclear} as the sum of T_{nuclear} and V_{nuclear} , where

$$T_{\text{nuclear}} = -\frac{\hbar^2}{2m} \sum_i^N \nabla_{\mathbf{R}_i}^2 + \frac{\hbar^2}{2I} \sum_i^N \mathbf{L}_i^2, \quad (1)$$

and

$$V_{\text{nuclear}} = \frac{1}{2} \sum_{i \neq j}^N V_{\text{pair}}(\mathbf{R}_{ij}, \boldsymbol{\Omega}_i, \boldsymbol{\Omega}_j). \quad (2)$$

Here \mathbf{R}_i is the center-of-mass position vector of the i th molecule, $\boldsymbol{\Omega}_i$ its orientation vector, \mathbf{L}_i its angular momentum operator, and the intermolecular separation vector $\mathbf{R}_{ij} \equiv \mathbf{R}_i - \mathbf{R}_j$. The molecular mass and moment of inertia are denoted by m and I , respectively. For a linear molecule with the intramolecular bond length fixed, I is a scalar constant. The values of $m = 3676$ and 7352 (atomic units) for H_2 and D_2 , respectively, and rotational constants $B \equiv \hbar^2/2I = 84.98$ and 42.92 K for H_2 and D_2 , respectively, are used.^{33,39} Among the the nuclear degrees of freedom, we include both translation and rotation modes of molecules in the kinetic energy T_{nuclear} ,

but we consider implicitly the intramolecular vibration mode along with the electronic degrees of freedom by judiciously choosing V_{pair} the pair-wise sum of which gives the potential energy V_{nuclear} .

We have enough evidence to support the present approach in our research range ($0 \sim 200$ GPa and $0 \sim 1000$ K). First, we can neglect the molecular dissociation, because its fraction is less than 0.01% from the same analysis as the one leading to about 5% at 140 GPa and 3000 K.^{10,40} Secondly, *ab initio* quantum-chemistry calculations at $N=2$ lead us to the conclusion that the dependence of V_{pair} on the bond length r_0 is weak, even though r_0 shrinks by more than 10% from 1.4 bohr (0.74\AA) as two H_2 molecules come closer.⁴¹ This assures the validity to employ an r_0 -independent V_{pair} . The notion of V_{pair} is relevant if r the intermolecular distance is larger than about 2.3 bohr (1.2\AA), because each molecule is estimated to possess a repulsive core of the radius of 0.6\AA .¹¹ Finally the effect of zero-point intramolecular vibrations (vibrons) can be taken into account in the form of V_{pair} as we shall illustrate in Sec. IV by using a toy model.

B. H_2 - H_2 interaction

Rather than determining V_{pair} from first principles, we shall resort to a phenomenological approach which is well reviewed in the literature.^{39,42} In general, the multi-dimensional function $V_{\text{pair}}(\mathbf{R}_{12}, \boldsymbol{\Omega}_1, \boldsymbol{\Omega}_2)$ can be expressed as the sum of the isotropic pair potential $V_0(R_{12})$ and the anisotropic potential $V_{\text{ani}}(\mathbf{R}_{12}, \boldsymbol{\Omega}_1, \boldsymbol{\Omega}_2)$. A variety of analytic forms have been proposed for $V_0(R)$ and their relevance has been tested in the past. Four of them are illustrated in Fig. 1. Because the Lennard-Jones (LJ) two-parameter form (the dotted-dashed curve in Fig. 1) has an unphysically strong repulsive core, more sophisticated forms have been proposed. The most commonly used form is either BUCK potential V_{BUCK} ⁴² or SG potential V_{SG} ,⁴³ plotted by dashed and dotted curves, respectively, in Fig. 1. Although they have almost the same analytic form, V_{BUCK} is fitted to the gas-phase data, while V_{SG} to the solid-phase data. In order to include the three-body interactions effectively in the solid environment, a further refinement is introduced to the original form of V_{SG} by incorporating an additional repulsive term, leading to the final form of SG potential. Compared to V_{BUCK} , the net effects contributed from the three-body interaction are a hardening of V_{SG} at small R and a slight raising of the well depth. Their concrete forms can be found in Refs. 37,39, and 42.

This $V_{\text{SG}}(R)$ works well for the solid H_2 and D_2 under ambient pressures. Under high pressures, however, an additional softening effect found by Hemley *et al.* is needed to correctly describe the enhanced many-body contributions in the short-range region caused by the dense solid environment. This effect can be incorporated by an *ad hoc* short-range correction $V_{\text{SR}}(R)$ to $V_{\text{SG}}(R)$,³⁸ leading

to the definition of the Hemley-corrected SG potential $V_{\text{SGH}}(R)$ (the solid curve in Fig. 1), where the actual form of $V_{\text{SR}}(R)$ can be found in Refs. 37 and 38. This softening correction at small R is very important in reproducing the equation of state (EOS) derived experimentally from the liquid D_2 shock-wave data,^{45,46} as assessed by Cui *et al.* in Ref. 37 in which the EOS for D_2 at $T = 20\text{K}$ and for P up to 40GPa is calculated for testing the intermolecular potential. From the test, the EOS is proved to be insensitive to the details of V_{ani} , but it is very sensitive to the choice of $V_0(R)$ which controls the translational motion of molecules. In fact, $V_{\text{SGH}}(R)$ gives results in excellent agreement with the experimental data,³⁸ while $V_{\text{SG}}(R)$ does not. The same conclusion is also drawn at $T = 300\text{K}$ from a similar test; for P up to 200GPa, $V_{\text{SGH}}(R)$ provides the results for the EOS in line with the experimentally obtained fitting formula.³⁷

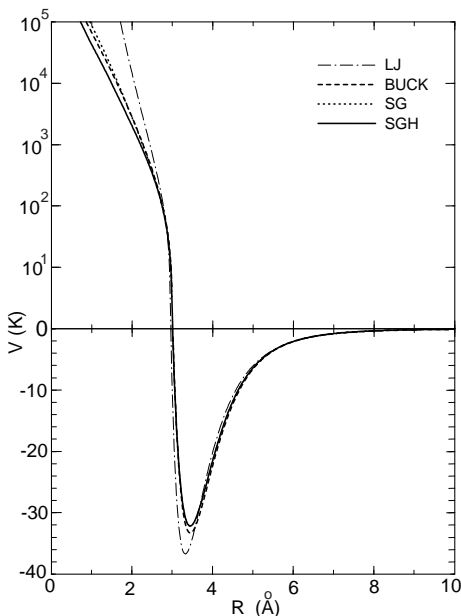


FIG. 1. Various potentials proposed for the interaction between two H_2 molecules. The solid, dotted, dashed, and dotted-dashed curves represent, respectively, the SGH, SG, BUCK, and LJ potentials.

Only a few works have been done for the assessment of V_{ani} . Using the *ab initio* quantum chemical method to evaluate the contributions such as the long-range electronic quadrupole-quadrupole interaction and the atom-diatom scattering term, Schaefer *et al.* have given a potential for V_{ani} .^{47–49} Comparing the results obtained from the electronic-structure calculation in the LDA, Runge *et al.* have found that this Schaefer potential V_{Schaefer} is too repulsive in the dense solid. Thus, in order to soften it, they have introduced a scaling factor to V_{Schaefer} to provide V_{ani} as $\alpha_n V_{\text{Schaefer}}$.³³ This factor α_n is linear in the nearest neighbor spacing R_{nn} to correctly describe the dense-solid environment as $\alpha_n = 0.61 + 0.31(R_{nn}/R_{nn}^0 - 0.5)$ with $R_{nn}^0 = 3.789\text{Å}$, the H_2 equi-

librium zero-pressure nearest-neighbor spacing. Both the bare V_{Schaefer} and the scaled one for V_{ani} have been tested in Ref. 37 to find that this difference is crucial in reproducing the I/II phase line for the solid D_2 . The best agreement with the experimental data for P up to 150GPa is achieved by using the scaled anisotropic potential combined with $V_{\text{SGH}}(R)$ for $V_0(R)$. The bare V_{Schaefer} predicts the transition to occur at much lower pressures. This difference was also observed in the fixed-lattice PIMC study.³³

For those reasons mentioned above, we shall choose the sum of $V_{\text{SGH}}(R)$ and the scaled Schaefer potential as V_{pair} in this paper. We believe that this V_{pair} is most reliable for the study of solid molecular H_2 and D_2 in our research range, in particular, for $P < 150\text{GPa}$.

C. Path Integral Monte Carlo method with constant pressure ensemble

With the Hamiltonian thus provided, we model the bulk solid by a simulation cell, which is periodically duplicated in all three spatial dimensions to minimize surface and finite-size effects. Initial size and geometry of the simulation cell are chosen to accommodate a particular number of molecules (N) and hcp structure. Our calculations are performed mostly on $N = 288$ and from an initial simulation cell determined by two basis vectors (\mathbf{a}_p and \mathbf{b}_p) forming a 60° angle and by the third one (\mathbf{c}_p) perpendicular to them with the length ratio of $a_p : b_p : c_p = 1 : 1 : 4\sqrt{6}/9$. The packing pattern is ABAB... to form the hcp lattice structure. Extensive testing on $N = 96, 150$ and 392 has also been made.

In studying the effect of heating solid H_2 isobarically at high pressures, we perform the path-integral Monte Carlo calculations with a constant-pressure (NPT) ensemble, instead of a simpler constant-volume (NVT) one, to avoid a bias of the restrictive cell geometry with a predetermined crystal structure. Implementation of the NPT ensemble is achieved by extra independent Metropolis moves of three basis vectors \mathbf{a}_p , \mathbf{b}_p and \mathbf{c}_p , which generates a Markov chain of states having a limiting distribution proportional to $\exp(-H/T + N \ln V)$ at T with the enthalpy $H(= PV + E_s)$, where E_s is the energy expectation value $\langle H_{\text{nuclear}} \rangle$ of the configuration s with s representing a set of scaled coordinates. This enables us to monitor volume changes and therefore to observe a possible first-order phase transition directly.

In order to avoid the “minus-sign problem” in QMC studies inherent in fermions, we confine ourselves to studying $p\text{-H}_2$ and $o\text{-D}_2$. After 4000 Monte Carlo steps for equilibration, statistical averages are collected from every second step, to a total of about 4000 data points. Because we focus on higher temperatures than the room temperature, relatively smaller partition number in the imaginary-time axis (M) is enough. At a fixed P , we start with simulations at the room temperature at which

M is increased up to 16 to ensure the convergence. We come to know that $M = 8(5)$ is enough for $P = 30\text{GPa}$ (higher P). Once its large enough value is determined, M is held fixed during heating at the given P . This allows us to use the equilibrium configuration at low temperature as a start-up one for higher temperature, resulting in continuous heating of our sample. Because other computation techniques are documented in Ref. 37, we omit further details of them here.

III. RESULTS

We observe the equilibrium structure in real space directly and also monitor the pair distribution function $g(R)$ that represents the conditional probability of finding other molecules at the distance R from a specified molecule at the origin:

$$g(R) = \frac{1}{4\pi R^2 \rho} \left\langle \sum_{i < j} \delta(R_{ij} - R) \right\rangle, \quad (3)$$

with ρ the density of system. This function shows a set of well-defined peaks characteristic to the configuration of neighboring molecules around the one at the origin. The function $O(R)$ defined in Ref. 37 is used to measure the correlation in molecular orientation.

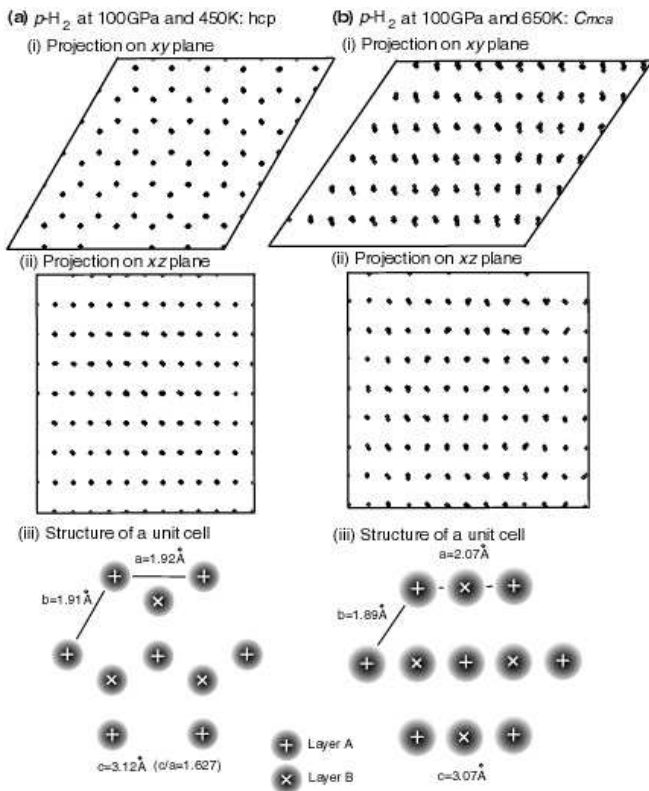


FIG. 2. Snapshots of the average equilibrium distribution of molecules at 100GPa in real space projected on both (i) xy and (ii) xz planes. Row (a): $p\text{-H}_2$ at 450K; row (b): $p\text{-H}_2$ at 650K. The structure of each unit cell is shown in (iii) in which the size of fluctuations is represented by the painted region.

The equilibrium distribution of 288 ($= 6 \times 6 \times 8$) molecules in real space projected on both xy and xz planes are shown in Fig. 2 for $p\text{-H}_2$ at 100GPa and at two different temperatures. Although it fluctuates with the standard deviation indicated by the painted region in Fig. 2(iii), on the average, each molecule occupies the lattice site of hcp at 450K, while that of an orthorhombic $Cmca$ structure at 650K.

For detecting this transition quantitatively, we plot $g(R)$ at $P = 100\text{GPa}$ with the increase of T in Fig. 3. Below 560K the second peak in $g(R)$ at $R \sim 2.72\text{\AA}$, a characteristic feature of hcp, is clearly seen. But the peak disappears at higher T , which is a sign of the structural transition from hcp to $Cmca$. Thus we identify the transition temperature T_{tr} as 560K with a statistical error of 20K. (By “statistical” we mean that the difference of states cannot be seen clearly if that in T is less than 20K due to statistical fluctuations.) This structural change is always seen in the system with $N = 96, 150,$ or 392. We find a large N dependence of T_{tr} , leading to an error of 40K or larger incurred at extrapolation of T_{tr} at $N \rightarrow \infty$. This error cannot be reduced further, because calculations with a much larger N are not feasible at present.

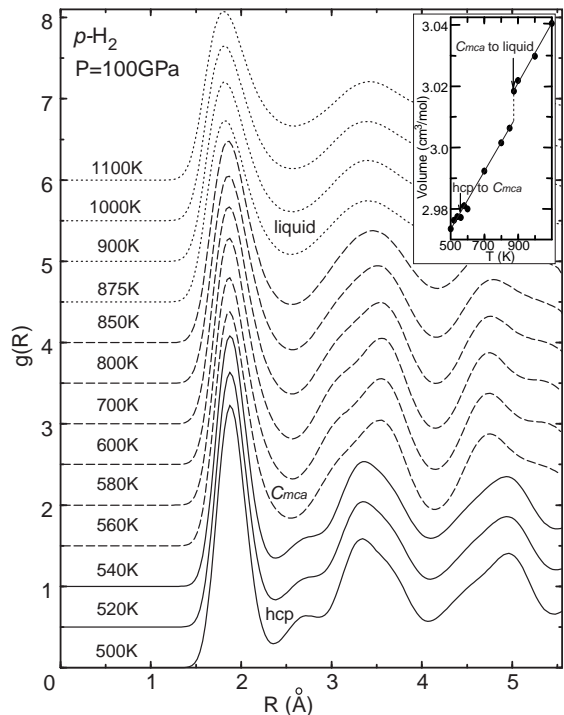


FIG. 3. Temperature dependence of $g(R)$ for $p\text{-H}_2$ at 100GPa. Inset shows the temperature dependence of volume. (Statistical errors are smaller than the size of symbols.)

With the further increase of T from T_{tr} , the peaks in $g(R)$ become less sharp. Eventually at T above 875K (which we identify the melting temperature T_m with a statistical error of 25K, about the same size of an error due to extrapolation in $N \rightarrow \infty$) $g(R)$ exhibits characteristics of a liquid phase. This first-order melting transition can be much better identified by the discontinuous change with T in either the enthalpy H or volume V (the inset of Fig. 3).

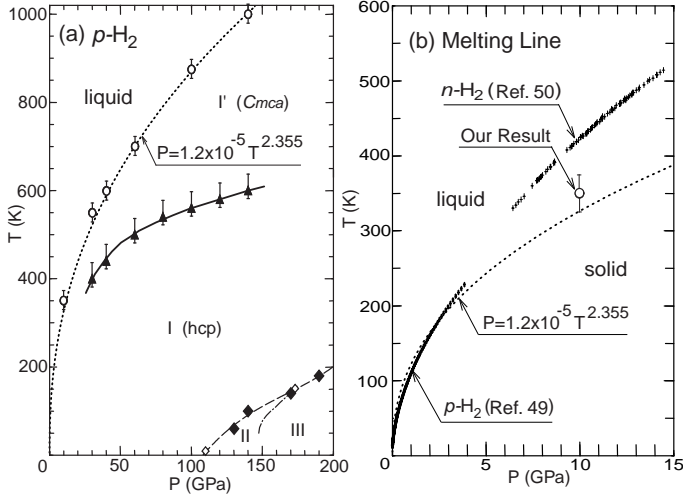


FIG. 4. (a) Phase diagram of p -H₂. At low temperatures, the dashed curve shows the I/II phase boundary interpolated through the two measured data marked by open diamonds (Refs. 4 and 7), while the dotted-dashed curve indicates the experimental II/III phase boundary. Solid diamonds represent the orientational order-disorder phase transition points obtained by PIMC in Ref. 37. (Size of the symbols represents the magnitude of errors.) Solid triangles and open circles for the hcp/ $Cmca$ transition and the melting, respectively, show the new phase boundaries obtained in this study. The dotted curve is a Simon fit to the melting line of this work. (b) Melting line at low pressures with experimental data for n -H₂ (pluses)⁵¹ and for p -H₂ (stars).⁵⁰

By evaluating both T_{tr} and T_m at other pressures, we obtain the phase diagram of dense p -H₂ in the T - P plane as shown in Fig. 4(a). The new solid phase is labeled as phase I'. Since $O(R)$ vanishes, its structure is orientationally disordered. The I'/I and liquid/I' phase boundaries are indicated by solid triangles and open circles with error bars, respectively. Large curvature of the phase line for $P < 50$ GPa reflects the rapid change of the volume in that region. A Simon equation of $P = 1.2 \times 10^{-5} T_m^{2.355}$ (the dotted curves in Fig. 4) fits our results rather well. A lack of experiment on T_m at high pressures makes a precise comparison between theory and experiment difficult, but we obtain a reasonably good agreement with the data⁵⁰ for $P < 4$ GPa, as can be seen in Fig. 4(b). The data for n -H₂ up to 15 GPa,⁵¹ are always higher than our results, reflecting the fact that the presence of o -H₂ makes T_m higher.⁵⁰ In Fig. 5(a) we show our result for dense o -D₂ exhibiting a similar phase diagram. The difference in

T_{tr} between these two systems becomes smaller with the increase of P , but p -H₂ gives definitely a higher T_{tr} than o -D₂. As for T_m , we find no meaningful difference.

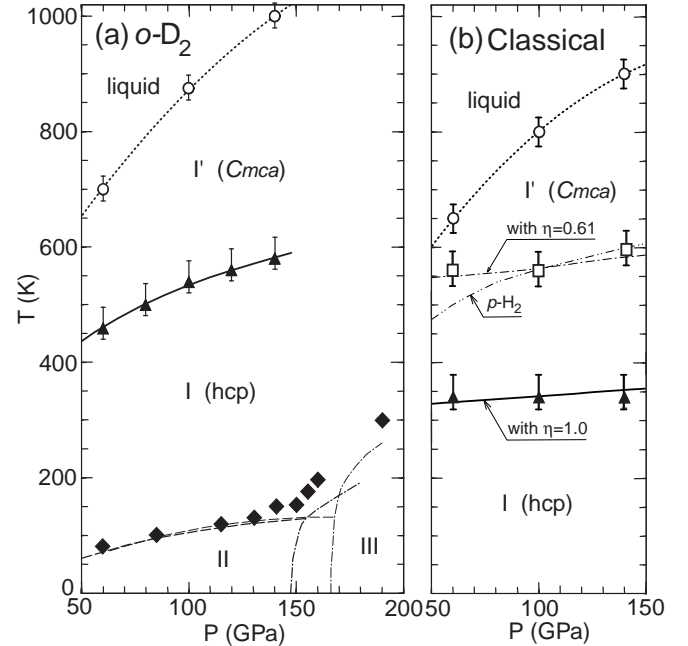


FIG. 5. (a) Similar phase diagram for o -D₂ with symbols indicating just the same meanings as those in Fig. 4(a). Two sets of experiments have detected three distinct phases I, II, and III for P below 200 GPa at low temperatures, as indicated by two dashed and dotted-dashed curves with different thickness, taken from Refs. 3 and 7. In (b), solid triangles are the corresponding high-temperature phase transition points for the classical reference system ($M = 1$), while open squares show the transition points by the pair potential with $\eta = 0.61$, defined in Eq. (8). (See the text in Sec. IV.) For comparison's sake, the double-dotted-dashed curve shows the data for solid H₂, the same as in Fig. 4 (a).

IV. QUANTUM HARDENING EFFECT

For understanding the mechanism to bring about the phase I', we have performed another simulation with $M = 1$ (the "classical reference" system in which the molecules are treated as classical particles) and found an analogous phase diagram as shown in Fig. 5(b). In this system, only the temperature-induced random motion of molecules can play a role in transforming a compact hcp structure into a less compact $Cmca$ one and finally into a liquid. Thus we can identify the thermal fluctuations as the basic driving force of the present phase transition.

Examining the changes of various physical quantities at T around T_{tr} , we found that the most important change occurs in the potential energy. The energy increases with T in both the classical (Fig. 6(a)) and the H₂ (Fig. 6(b)) systems due primarily to the fluctuation of molecules to shorten the nearest-neighbor distance $R_0 \sim 1.9\text{\AA}$, because V_{pair} is very repulsive at R near R_0 and it changes

very rapidly with R . (See Fig. 1.) We should note that the increasing rate is larger in the compact hcp phase than that in the less compact $Cmca$ phase. In this regard, the phase transition is induced by the potential-energy gain as indicated in Fig. 6. No such gain is seen for the translational kinetic energy as shown in the inset of Fig. 6(b).

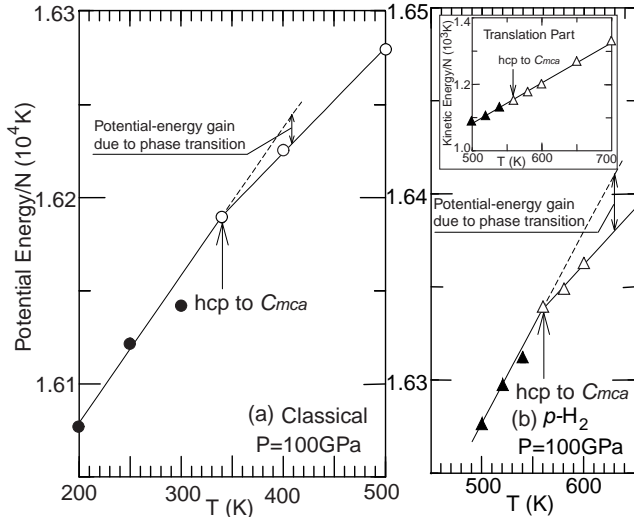


FIG. 6. Temperature dependence of the potential energy (V_{nuclear}) per molecule for both (a) the classical reference system and (b) $p\text{-H}_2$ near respective T_{tr} 's at 100 GPa. Data in hcp and $Cmca$ structures are shown by solid and open symbols, respectively. The inset in (b) plots the change in the translational kinetic energy per molecule.

Eventually the reason why T_{tr} in the classical system is much lower than that in solid $p\text{-H}_2$ must be ascribed to the quantum zero-point motion of protons, the only ingredient that is not included in the classical system. Such a motion is, in a sense, regarded as a kind of vacuum polarization the effect of which, in the context of high-energy physics, can be renormalized into fundamental physical quantities such as mass and interaction constant. We envisage that this must also be the case here. In order to substantiate this, we consider a toy model, namely, an interacting two-particle system in a harmonic potential in one dimension, described by the Hamiltonian as

$$H = \frac{p_1^2}{2m} + \frac{Kx_1^2}{2} + \frac{p_2^2}{2m} + \frac{Kx_2^2}{2} + V(x_1 - x_2), \quad (4)$$

from which we can derive the Hamiltonian for the relative motion as

$$H_r = \frac{p^2}{2\mu} + \mu\omega^2 x^2 + V(x), \quad (5)$$

where $\mu = m/2$, $\omega = \sqrt{K/2\mu}$ and $x = x_1 - x_2$. By writing $\psi(x) = \psi_0(x)\varphi(x)$ and $E = \omega/2 + \varepsilon$ with $\psi_0(x) = \sqrt[4]{\mu\omega/\pi} \exp(-\mu\omega x^2/2)$, we can cast Eq. (5) into

$$\left(\frac{p^2}{2\mu} + \tilde{V}(x)\right)\varphi(x) = \varepsilon\varphi(x), \quad (6)$$

where the effective interaction $\tilde{V}(x)$ is related to the bare one through

$$\tilde{V}(x) \equiv V(x) - \mu^{-1} \frac{\psi_0'}{\psi_0} \frac{\varphi'}{\varphi} = V(x) + \omega x \frac{\varphi'}{\varphi}, \quad (7)$$

We see that the effect of the zero-point oscillation is included effectively in $\tilde{V}(x)$, implying that the physics can be captured in terms of $\tilde{V}(x)$.⁵² In this sense, V_{pair} can include the effect of intramolecular vibrons.

In general the closed-packed structure is known to become more stable with a harder V_{pair} .⁵³ In the above toy model, we readily know that, if $V(x)$ is repulsive, $x\varphi'/\varphi$ is positive, leading $\tilde{V}(x)$ to be more repulsive than $V(x)$. This indicates that the zero-point motion of protons can make V_{pair} effectively more repulsive than that in the classical system in which $\tilde{V}(x)$ is reduced to $V(x)$ owing to $\omega = \sqrt{K/m} \rightarrow 0$ as $m \rightarrow \infty$.

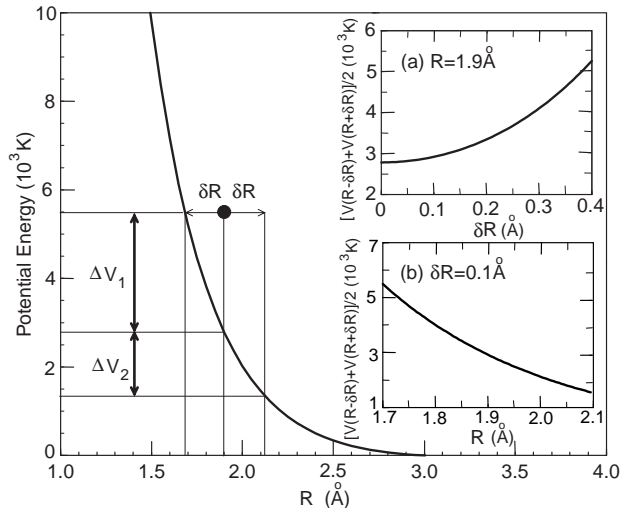


FIG. 7. Schematic view to understand the Fluctuation effect on the potential energy. Inset: (a) average potential energy as a function of fluctuation δR with $R = 1.9 \text{ \AA}$. (b) average potential energy as a function of separation R with $\delta R = 0.1 \text{ \AA}$.

This hardening effect due to the molecular fluctuations can be understood more visually through Fig. 7. At the pressure range considered in this paper, the repulsive part of the interaction plays a central role in determining the potential energy. The fluctuation shortens one distance between the neighboring molecules, but at the same time it lengthens another one. Thus we have to average these two opposite effects. Because the potential changes very rapidly with R the intermolecular distance, ΔV_1 the increase of the potential due to the shortening is larger than ΔV_2 the decrease due to the lengthening. Therefore the average potential energy, $[V(R - \delta R) + V(R + \delta R)]/2$, becomes larger than $V(R)$ the potential energy without

the fluctuation. As shown in the inset (a) of Fig. 7, the larger the fluctuation, the more repulsive the potential energy. This explains the behavior of the potential energy in Fig. 6; the solid H₂ has a larger potential energy than the classical reference system at the same pressure and temperature, because it provides larger fluctuations due to the combination between the quantum and thermal effects. This also manifests itself in the much larger potential-energy gain in Fig. 6(b) than that in Fig. 6(a). Thus we can conclude that the molecules in the quantum system feel an effectively more repulsive potential than those in the classical system. This “quantum hardening effect” of V_{pair} explains why hcp becomes more stable in p -H₂.

With the increase of pressure, the deviation of the I/I' phase lines between solid H₂ and the classical system is getting larger. In order to understand this result, we plot $[V(R - \delta R) + V(R + \delta R)]/2$ as a function of R with a given δR in the inset (b) of Fig. 7. The average potential energy increases with the decrease of R , a behavior of R seen with the increase of pressure. Thus we conclude that the quantum hardening effect becomes stronger with increasing pressure and this explains the above result well.

In order to study this quantum hardening effect more quantitatively, we have performed another simulation in the classical system with the pair potential, defined as

$$V_{\text{pair}} = V_{\text{SG}} + \eta V_{\text{SR}} + V_{\text{ani}}, \quad (8)$$

where the parameter η is introduced to measure the softness of V_{pair} ; $\eta = 0$ for the hardest SG potential and $\eta = 1$ for the softest SGH one. In Fig. 5(b), the open squares with error bars show the I/I' phase boundary obtained using V_{pair} with $\eta = 0.61$. Notice that this more repulsive potential than the SGH one makes the I/I' phase boundary of the reference classical system almost the same as the one for the quantum solid H₂ with the SGH potential (the double-dotted-dashed curve) at $P = 100$ GPa. We need a softer (harder) V_{pair} to better fit the data at lower (higher) pressure, but this behavior is consistent with the above-mentioned pressure dependence of the quantum hardening effect.

V. SUMMARY

Utilizing an intermolecular interaction potential V_{pair} proved to be reliable at high pressures in the PIMC simulations, we have found the structural phase transition from orientationally disordered hcp to *Cmca* induced by thermal fluctuations in both dense solid H₂ and D₂ before melting. The result shows that a new phase exists at high temperatures in the solid molecular systems. The potential-energy gain due to the enhancement of fluctuations with increasing temperature is the main source to bring about the structural phase transition. The strong quantum zero-point motion plays an important role in determining T_{tr} the transition temperature through the

quantum hardening effect on the potential energy. The melting temperature T_m is also estimated for full understanding the behavior of the solids and for the evaluating the temperature range of the new phase.

Through additional simulation studies, we have also examined to see how our conclusion about the existence of the new phase is robust against the choice of V_{pair} . We have found that both T_{tr} and T_m are rather sensitive to the change of V_{pair} . An example of T_{tr} is given in Fig. 5(b). However, there is always a melting transition *after* the I/I' transition with increasing temperature, suggesting the robustness of the existence of the *Cmca* phase.

ACKNOWLEDGMENTS

This work is supported by Chinese National Foundation for Doctoral Education, Scientific Research Foundation for Returned Overseas Chinese Scholars, Chinese National Natural Science Foundation, and Japanese Monbusho Scholarship for Exchange Visiting Researchers.

-
- ¹ E. Wigner and H. B. Huntington, J. Chem. Phys. **3**, 764 (1935).
 - ² C. Narayana, H. Luo, J. Orloff, and A. L. Ruoff, Nature **393**, 46 (1998).
 - ³ H.-K. Mao and R. J. Hemley, Rev. Mod. Phys. **66**, 671 (1994).
 - ⁴ L. Cui, N. H. Chen and I. F. Silvera, Phys. Rev. **B51**, 14987 (1995).
 - ⁵ A. F. Goncharov, I. I. Mazin, J. H. Eggert, R. J. Hemley, and H. K. Mao, Phys. Rev. Lett. **75**, 2514 (1995).
 - ⁶ R. J. Hemley, H. K. Mao, A. F. Goncharov, M. Hanfland, and V. Struzhkin, Phys. Rev. Lett. **76**, 1667 (1996).
 - ⁷ I. I. Mazin, R. J. Hemley, A. F. Goncharov, M. Hanfland, and H.-K. Mao, Phys. Rev. Lett. **78**, 1066 (1997).
 - ⁸ N. H. Chen, E. Sterer, and I. Silvera, Phys. Rev. Lett. **76**, 1663 (1996).
 - ⁹ L. Cui, N. H. Chen, and I. F. Silvera, Phys. Rev. Lett. **74**, 4011 (1995).
 - ¹⁰ S. T. Weir, A. C. Mitchell, and W. J. Nellis, Phys. Rev. Lett. **76**, 1860 (1996).
 - ¹¹ W. R. Magro, D. M. Ceperley, C. Pierleoni, and B. Bernu, Phys. Rev. Lett. **76**, 1240 (1996).
 - ¹² B. Militzer and E. L. Pollock, Phys. Rev. **E61**, 3470 (2000).
 - ¹³ N. W. Ashcroft, Phys. Rev. Lett. **21**, 1748 (1968).
 - ¹⁴ C. Friedli and N. W. Ashcroft, Phys. Rev. **B16**, 662 (1977).
 - ¹⁵ T. W. Barbee III, A. Garcia, M. L. Cohen, and J. M. Martin, Phys. Rev. Lett. **62**, 1150 (1989).
 - ¹⁶ E. Kaxiras, J. Broughton, and R. J. Hemley, Phys. Rev. Lett. **67**, 1138 (1991).
 - ¹⁷ E. Kaxiras and J. Broughton, Europhys. Lett. **17**, 151 (1992).

- ¹⁸ H. Nagara and T. Nakamura, Phys. Rev. Lett. **68**, 2468 (1992).
- ¹⁹ M. P. Surh, T. W. Barbee III, and C. Mailhot, Phys. Rev. Lett. **70**, 4090 (1993).
- ²⁰ B. Edwards, N. W. Ashcroft, and T. Lenosky, Europhys. Lett. **34**, 519 (1996).
- ²¹ M. P. Surh, K. J. Runge, T. W. Barbee III, E. L. Pollock, and C. Mailhot, Phys. Rev. B **55**, 11330 (1997).
- ²² K. Nagao and H. Nagara, Phys. Rev. Lett. **80**, 548 (1998).
- ²³ K. Nagao, T. Takezawa, and H. Nagara, Phys. Rev. **B59**, 13741 (1999).
- ²⁴ K. A. Johnson and N. W. Ashcroft, Nature **403**, 632 (2000).
- ²⁵ M. Städele and R. M. Martin, Phys. Rev. Lett. **84**, 6070 (2000).
- ²⁶ J. Kohanoff and J.-P. Hansen, Phys. Rev. Lett. **74**, 626 (1995).
- ²⁷ J. Kohanoff, S. Scandolo, G. L. Chiarotti, and E. Tosatti, Phys. Rev. Lett. **78**, 2783 (1997).
- ²⁸ J. Kohanoff, S. Scandolo, S. de Gironcoli, and E. Tosatti, Phys. Rev. Lett. **83**, 4097 (1999).
- ²⁹ H. Kitamura, S. Tsuneyuki, T. Ogitsu, and T. Miyake, Nature **404**, 259 (2000).
- ³⁰ D. M. Ceperley and B. J. Alder, Phys. Rev. B **36**, 2092 (1987).
- ³¹ V. Natoli, R. M. Martin, and D. Ceperley, Phys. Rev. Lett. **74**, 1601 (1995).
- ³² M. Zoppi and M. Neumann, Phys. Rev. **B43**, 10242 (1991).
- ³³ K. J. Runge, M. P. Surh, C. Mailhot, and E. L. Pollock, Phys. Rev. Lett. **69**, 3527 (1992).
- ³⁴ M. Wagner and D. M. Ceperley, J. Low Temp. Phys. **94**, 161 (1994).
- ³⁵ E. Kaxiras and Z. Guo, Phys. Rev. **B49**, 11822 (1994).
- ³⁶ M. Zoppi, U. Bafle, E. Guarini, F. Barocchi, R. Magli, and M. Neumann, Phys. Rev. Lett. **75**, 1779 (1995).
- ³⁷ T. Cui, E. Cheng, B. J. Alder, and K. B. Whaley, Phys. Rev. **B55**, 12253 (1997).
- ³⁸ R. J. Hemley et al., Phys. Rev. **B42**, 6458 (1990).
- ³⁹ I. Silvera, Rev. Mod. Phys. **52**, 393 (1980).
- ⁴⁰ N. C. Holmes, M. Ross, and W. J. Nellis, Phys. Rev. **B52**, 15835 (1995).
- ⁴¹ F. H. Ree and C. F. Bender, J. Chem. Phys. **71**, 5362 (1979).
- ⁴² U. Buck, F. Huisken, A. Kohlhasse, D. Otten, and J. Schaefer, J. Chem. Phys. **78**, 4439 (1983).
- ⁴³ I. Silvera and V. V. Goldman, J. Chem. Phys. **69**, 4209 (1978).
- ⁴⁴ W. Meyer, Chem. Phys. **104**, 3155 (1976).
- ⁴⁵ W. J. Nellis, A. C. Mitchell, M. van Thiel, G. J. Devine, R. J. Trainor, and N. Brown, J. Chem. Phys. **79**, 1480 (1983).
- ⁴⁶ M. Ross, F. H. Ree, and D. A. Young, J. Chem. Phys. **79**, 1487 (1983).
- ⁴⁷ J. Schaefer and W. Meyer, J. Chem. Phys. **70**, 344 (1979).
- ⁴⁸ L. Monchick and J. Schaefer, J. Chem. Phys. **73**, 6153 (1980).
- ⁴⁹ J. Schaefer and W. E. Köhler, Z. Phys. **D13**, 217 (1989).
- ⁵⁰ A. Driessen, J. A. de Waal, and I. F. Silvera, J. Low Temp. Phys. **34**, 255 (1979).
- ⁵¹ F. Datchi, P. Loubeyre, and R. LeToullec, Phys. Rev. **B61**, 6535 (2000).
- ⁵² In this toy model, the zero-point oscillation is considered in a harmonic potential due to the simplifying fact that an analytic expression for $\psi_0(x)$ is known. Even if it cannot be described well by a harmonic potential, our conclusion still holds; if anharmonicity plays a role in the zero-point oscillation, we can easily include its effect by redefining $\psi_0(x)$ as the ground-state wavefunction for the system with the anharmonicity, leading to an equation in just the same form as in Eq. (6) with $\tilde{V}(x)$ defined by the first equation in Eq. (7). (Note that the second equation does not hold in this anharmonic case.)
- ⁵³ See, for example, D. G. Pettifor, *Bonding and Structure of Molecules and Solids*, Clarendon, Oxford, 1995.